Sensors and Actuators A 319 (2021) 112519

Contents lists available at ScienceDirect

Sensors and Actuators A: Physical

journal homepage: www.elsevier.com/locate/sna

Active atomic force microscope cantilevers with integrated device layer piezoresistive sensors

Michael G. Ruppert*, Andrew J. Fleming, Yuen K. Yong

University of Newcastle, Callaghan, NSW 2308, Australia

ARTICLE INFO

Article history:
Received 8 October 2020
Received in revised form 7 December 2020
Accepted 18 December 2020
Available online 18 January 2021

Keywords:
Atomic force microscopy
Active cantilevers
Microelectromechanical systems (MEMS)
Piezoelectric actuators
Piezoresistive sensors

ABSTRACT

Active atomic force microscope cantilevers with on-chip actuation and sensing provide several advantages over passive cantilevers which rely on piezoacoustic base-excitation and optical beam deflection measurement. Active microcantilevers exhibit a clean frequency response, provide a path-way to miniturization and parallelization and avoid the need for optical alignment. However, active microcantilevers are presently limited by the feedthrough between actuators and sensors, and by the cost associated with custom microfabrication. In this work, we propose a hybrid cantilever design with integrated piezoelectric actuators and a piezoresistive sensor fabricated from the silicon device layer without requiring an additional doping step. As a result, the design can be fabricated using a commercial five-mask microelectromechanical systems fabrication process. The theoretical piezoresistor sensitivity is compared with finite element simulations and experimental results obtained from a prototype device. The proposed approach is demonstrated to be a promising alternative to conventional microcantilever actuation and deflection sensing.

1. Introduction

The microcantilever is a microelectromechanical system (MEMS) that is a key enabling technology for atomic force microscopy (AFM) [1], scanning probe lithography systems [2], and probe-based data storage systems [3]. Due to the unprecedented resolution, AFM has significantly contributed to advances in chemistry [4], surface physics [5] and bio-nanotechnology [6].

In dynamic AFM, the cantilever is actively driven at one of its resonance frequencies while a sample is scanned underneath a sharp tip located at the oscillating end. By controlling changes in the oscillation amplitude using a feedback loop, 3D topography and maps of nanomechanical information can be obtained. While cantilever microfabrication technology has advanced over the years, the overall design has remained largely unchanged; a passive rectangular shaped cantilever design has been adopted as the industry standard. As a result, most conventional AFM systems employ piezoacoustic base-excitation [7] and an optical beam deflection (OBD) sensor [8] to induce and measure the corresponding vibration.

Piezoacoustic base-excitation is a straightforward method for exciting the microcantilever; however, this method also tends to excite resonance modes in the host structure, which results in the so-called 'forest of peaks'.

These additional dynamics render the tuning, analysis and identification of the cantilever response spectrum exceedingly difficult [9]. On the other hand, electrothermal actuation [10] or piezoelectric actuation [11] can be directly integrated on the cantilever chip level and have enabled single-chip MEMS atomic force microscopy [12,13].

Most conventional AFM systems rely on measuring the cantilever deflection using the optical beam deflection (OBD) method [8]. However, the optical measurement can require tedious laser alignment and mandates a sufficiently large cantilever with a reflective surface for optimal signal transduction. Additionally, imaging artifacts can occur from optical interference [14] and the method is not easily extendable to arrays for multi-probe configurations [15]. In contrast, an integrated strain-based deflection measurement such as piezoelectric [16] and piezoresistive sensing [17] offers several advantages [18] including a highly compact measurement setup, the potential for up-scaling to cantilever arrays [19], and improved sensitivity for small cantilevers [20] especially when measuring higher order eigenmodes [21,22].

Currently, fully integrated cantilevers can be fabricated using either piezoelectric (PE) or electrothermal (ET) actuation and using

* Corresponding author.
E-mail address: michael.ruppert@newcastle.edu.au (M.G. Ruppert).

https://doi.org/10.1016/j.sna.2020.112519
0924-4247/

Table 1
Comparison of fully integrated cantilevers (PE: piezoelectric, PR: piezoresistive, ET: electrothermal).

Ref.	Actuation	Sensing	Dynamic Range	Coupling	Fabrication
[30]	PE	PR	40 dB	DC	Custom
[31]	ET	PR	17 dB	DC	Custom
[22]	PE	PE	35 dB	AC	Standard
[29]	PE	PE	35 dB	AC	Custom
This Work	PE	PR	33 dB	DC	Standard

either piezoelectric or piezoresistive (PR) sensing. In order to minimize the MEMS fabrication steps and associated cost, a number of active cantilever designs have emerged which utilize piezoelectric transduction for both actuation and sensing [23,21,24,22,25]. These designs employ multiple laterally arranged piezoelectric transducers using the direct and indirect piezoelectric effect. However, this approach has a major draw-back since inevitable parasitic capacitances between the actuator and sensor create significant feedthrough [26] that can conceal the mechanical dynamics of the cantilever [24]. While this problem can be alleviated using active feedthrough cancellation [27,9,24,28], it requires significant manual tuning and is only effective in a narrow bandwidth around the resonance [9]. Recently, a piezoelectric cantilever design was proposed that improved feedthrough by arranging the piezoelectric transducers vertically [29] albeit by increasing the cost and complexity of the fabrication.

The feedthrough issue can be significantly reduced by separating the actuation and sensing principle [30,10,31,32,18]. However, incorporating multiple active regions during MEMS fabrication is not possible in standard commercial MEMS processes; and therefore, incurs a high cost or requires specialized facilities. Table 1 compares selected works on fully integrated cantilever designs and evaluates the designs based on dynamic range, coupling (usable frequency range) and required fabrication capability. Here, dynamic range is defined as the amplitude difference at resonance vs. off resonance and is used as a metric for feedthrough performance. The term ‘standard’ fabrication refers to the commercially available process PiezoMUMPS® by MEMSCAP Inc. It can be seen that while good dynamic range has been achieved with both standard and custom fabrication processes and piezoelectric actuation and sensing [22,29], this approach is limited in the usable frequency range. The highest dynamic range has been achieved with piezoelectric actuation and piezoresistive sensing but requires a custom fabrication process [30]. In comparison, this work achieves a high dynamic range without limitation in the usable frequency range and can be implemented with a standard fabrication process.

2. Contribution

In this work, we propose a cantilever design with piezoelectric actuators and a piezoresistive sensor which has the potential to maximize dynamic range (i.e. minimize feedthrough) while maintaining compatibility with a standard commercial fabrication process (PiezoMUMPS® MEMSCAP Inc.). To maintain fabrication compatibility, the need for an additional piezoresistor doping step must be avoided. In this work, this is achieved by utilizing the piezoresistive property of the silicon device layer, which has been previously exploited for displacement sensing in nanopositioners [33]. The proposed approach has the following benefits over existent technologies: (1) the separation of transduction principles achieves a low actuator-sensor feedthrough, (2) a standard commercial fabrication process can be used and (3) piezoresistive sensing has the capability to measure cantilever deflections down to DC (as opposed to piezoelectric sensing that can only measure AC deflections, compare Section 7.1).

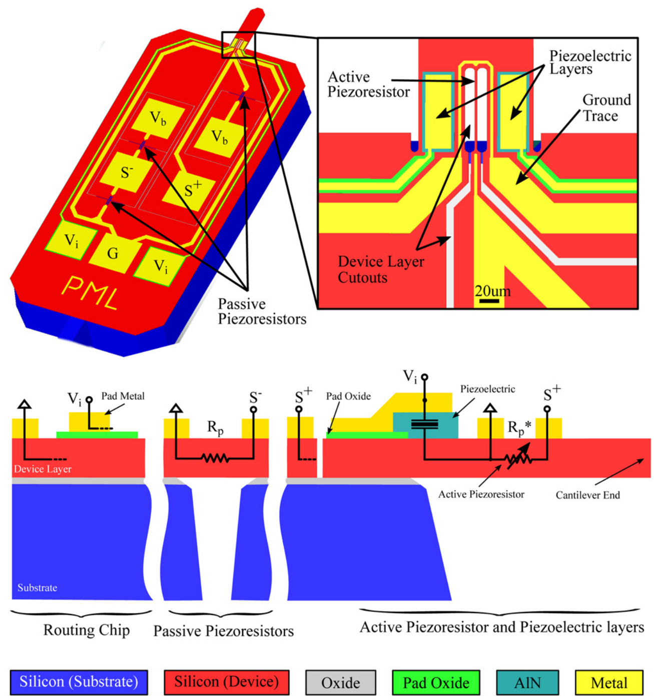

Fig. 1. Top and cross sectional view of the piezoelectric-piezoresistive cantilever MEMS design.

Table 2
Cantilever and piezoresistor parameters.

Param.	Description	Value
l	Cantilever length	500 μm
w	Cantilever width	150 μm
t	Cantilever thickness	10 μm
l_p	Piezoresistor length	100 μm
w_p	Piezoresistor width	3 μm
R_p^*/R_p	Piezoresistor resistance	164.6 Ω
$\bar{\pi}_l$	Eff. long. PR coeff.	-26.27×10^{-11} Pa^{-1}
E	Young’s modulus	169 GPa
ν	Poisson’s ratio	0.28
G	Gauge factor	−44.4
V_b	Bridge bias voltage	1.25 V
A	Total circuit gain	2100

This work extends preliminary finite element simulations of this concept [34]. In this work, a fabricated prototype is presented and the sensor sensitivity and feedthrough performance are assessed experimentally and compared with finite element simulations. Finally, the device is equipped with a focused ion beam tip and used for atomic force microscopy. These results demonstrate the capability to image nanometer scale steps on highly oriented pyrolytic graphite (HOPG) as well as topography and material properties of a polymer-blend sample using phase contrast at the fundamental mode.

3. The piezoelectric-piezoresistive cantilever

3.1. Cantilever and piezoresistor design

The piezoelectric-piezoresistive (PE-PR) cantilever proposed in this work is shown in Fig. 1 with dimensions stated in Table 2. The design consists of two symmetric piezoelectric actuators that use aluminum nitride (AlN) as the active material. These are driven by the voltage V_i applied to the top electrodes. To measure the out-of-plane deflection, a piezoresistive sensing beam is formed from the n-type doped silicon device layer using the device layer cut-

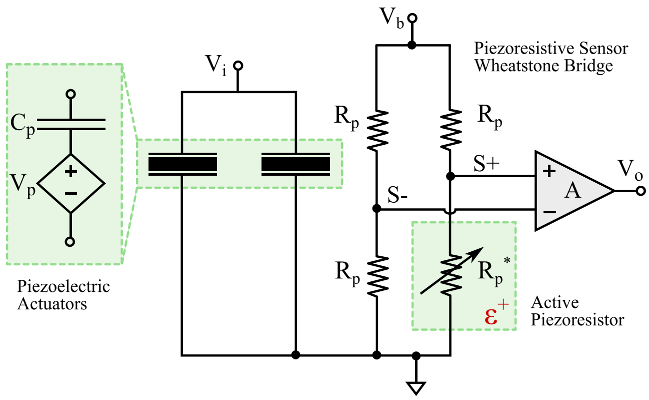

Fig. 2. Equivalent electrical circuit of the piezoelectric actuation and piezoresistive 1/4 Wheatstone bridge read-out configuration.

outs shown in Fig. 1. As a result, the piezoresistor shares a common node connected to ground with the piezoelectric actuators which dictates the 1/4 Wheatstone bridge configuration shown in Fig. 2. The value of the piezoresistor is given by the sheet-resistance of the n-type doped silicon device layer [35] and is chosen such that its thermal noise is similar to the first stage operational amplifier, as described in Section 4. To achieve closely matched resistor values to complete the Wheatstone bridge, three identical passive piezoresistive beams are incorporated on the cantilever chip. To achieve electrical isolation between all piezoresistors, the top device layer is removed on the cantilever chip.

3.2. Piezoresistive sensing

A cantilever with a piezoresistive element measures the strain in the element through a resistance change. This resistance change is given by

$$\frac{\Delta R}{R} = \frac{\Delta \rho}{\rho} + (1+2\nu)\varepsilon_l \approx \frac{\Delta \rho}{\rho} \tag{1}$$

where R is the electrical resistance, ρ the electrical resistivity, ν the Poisson's ratio, and ε_l the longitudinal strain. Here, the second term in (1) describes the resistance change due to the geometric effect, e.g. in a strain gauge. For silicon, this effect is usually one to two orders of magnitude smaller than the piezoresistive effect and can therefore be neglected [36]. The relative resistivity change is given by [37]

$$\frac{\Delta \rho}{\rho} = \pi_l \sigma_l + \pi_t \sigma_t \tag{2}$$

where σ_l and σ_t are the stress in the longitudinal (parallel to the current in the piezoresistor) and transverse (perpendicular to the current in the piezoresistor) direction and π_l and π_t are the corresponding longitudinal and transverse piezoresistive coefficients [38]. The value of these coefficients depends strongly on the doping type and the crystallographic orientation of the resistor. For a lightly doped ($10^{16}\,\mathrm{cm}^{-3}$) n-type single crystal silicon wafer in the (100) plane and a piezoresistor orientated along the $\langle 110 \rangle$ direction, the coefficients are given by [39]

$$\pi_l = \frac{1}{2}(\pi_{11} + \pi_{12} + \pi_{44}) = -31.6 \times 10^{-11}\,\mathrm{Pa}^{-1}, \tag{3a}$$

$$\pi_t = \frac{1}{2}(\pi_{11} + \pi_{12} - \pi_{44}) = -17.6 \times 10^{-11}\,\mathrm{Pa}^{-1}. \tag{3b}$$

Using the relationship between the longitudinal and the transverse stress $\sigma_t = -\nu\sigma_l$, (2) can be simplified to

$$\frac{\Delta \rho}{\rho} = \sigma_l(\pi_l - \nu\pi_t) = \bar{\pi}_l \sigma_l \tag{4}$$

where $\bar{\pi}_l$ is the effective longitudinal piezoresistive coefficient and ν is the Poisson's ratio [40] and are stated in Table 2.

The change in resistance is normally converted to a voltage signal using a DC Wheatstone bridge in either 1/4-bridge (1 active resistor) [17], 1/2-bridge (2 active resistors) [41] or a full bridge (4 active resistors) [42] configuration. The resistor in the same bridge arm as the active piezoresistor is usually chosen to counter-act the temperature dependence by using the same material and location. If a 1/4 Wheatstone bridge is used as shown in Fig. 2, the differential output voltage can be written as

$$V_d = S^+ - S^- = \left(\frac{R_p^*}{R_p^* + R_p} - \frac{R_p}{R_p + R_p} \right) V_b = \frac{\bar{\pi}_l \bar{\sigma}_l}{2(2 + \bar{\pi}_l \bar{\sigma}_l)} V_b \tag{5}$$

where $R_p^* = R_p(1 + \bar{\pi}_l \bar{\sigma}_l)$, R_p^*/R_p is the resistance of the active/passive piezoresistors, and V_b is the bridge bias voltage. Note that the output voltage is non-linearly dependent on the average stress in the piezoresistor $\bar{\sigma}_l$. For small deflections, a first order Taylor approximation can be used to yield

$$V_d \approx \frac{1}{4} \bar{\pi}_l \bar{\sigma}_l V_b = \frac{1}{4} G \varepsilon V_b. \tag{6}$$

where G is the dimensionless gauge factor and ε the strain. Assuming an Euler-Bernoulli beam with homogeneous isotropic linear elastic material with constant cross section in pure bending, an analytical expression for $\bar{\sigma}_l$ can be derived (for details compare Appendix A) to provide the theoretical output voltage as

$$V_d = \frac{1}{4} \bar{\pi}_l \frac{3tE}{4l^3} (2l - l_p) z(l) V_b. \tag{7}$$

Using (7) and the parameters stated in Table 2, the theoretical piezoresistive deflection sensitivity is

$$\Psi_{\mathrm{PR,th}} = 1.60\,\mathrm{mV/nm}. \tag{8}$$

The theoretical stiffness of the cantilever is given by [43]

$$k_1 = \frac{Ewt^3}{4l^3} = 50.7\,\mathrm{N/m} \tag{9}$$

and the theoretical cantilever fundamental resonance frequency is given by [43]

$$f_1 = \alpha_1^2 \sqrt{\frac{EI}{\rho t w l^4}} = 55.04\,\mathrm{kHz} \tag{10}$$

where $\alpha_1 = 1.875$ is the solution to the Euler-Bernoulli beam equation for the first mode, $I = \frac{1}{12} w t^3$ is the moment of inertia and ρ is the density of silicon.

3.3. Finite element simulation

A finite element analysis of the PE-PR cantilever was performed using CoventorWare for which the 5-mask PiezoMUMPS® fabrication process has been modeled [35]. First, a modal analysis is performed to obtain the first mode dynamic parameters such as resonance frequency and dynamic stiffness. Then, a dynamic harmonic analysis is performed by driving the piezoelectric actuators at the resonance frequency to obtain the tip deflection at resonance and corresponding stress distribution along the piezoresistor. This allows calculation of the simulated tip deflection sensitivity.

Using modal analysis, the fundamental resonance frequency is found to be $f_1 = 56.55$ kHz and the normalized mode shape of the fundamental eigenmode is shown in Fig. 3(a). With the mode shape normalized to maximum unity deflection, the modal stiffness k_1 is estimated from the modal mass m_1 [44] and the relationship $2\pi f_1 = \sqrt{k_1/m_1}$ and is found to be $k_1 = 52.58$ N/m.

The corresponding normal elastic stress distribution in the y-direction is calculated using a dynamic harmonic analysis by

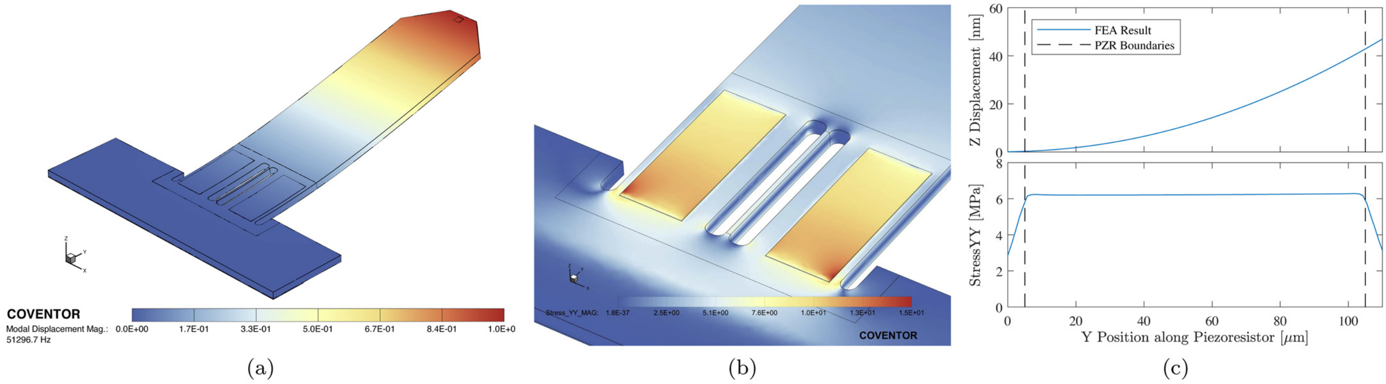

Fig. 3. Finite element simulation of the PE-PR cantilever using Coventor: (a) normalized deflection of the first mode, (b) normal elastic stress in the y-direction at the cantilever base for dynamic piezoelectric actuation at the first mode, and (c) displacement and stress profile along the piezoresistor length for the simulation in (b).

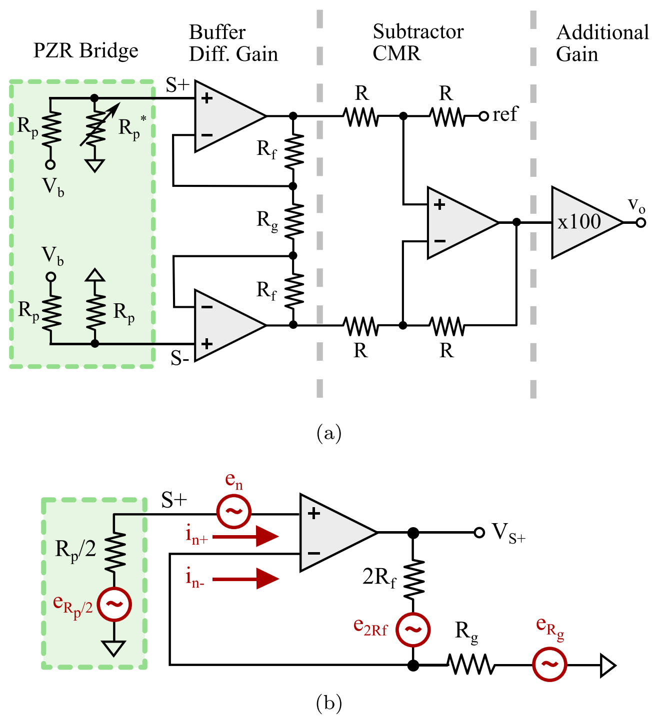

Fig. 4. (a) Instrumentation amplifier read-out configuration and (b) equivalent non-inverting amplifier noise circuit.

actuating the piezoelectric layers at the fundamental resonance frequency with 174.3 mV to yield a free-air amplitude of 580 nm. The results are shown in Fig. 3(b), focusing on the cantilever base and the piezoresistor where the highest stress concentration is found. The stress profile along the piezoresistor length is plotted in Fig. 3(c), which is observed to be approximately constant. On either side of the piezoresistor boundaries, the stress drops off steeply. For the simulated amplitude, the average surface stress over the piezoresistor length is $\bar{\sigma}_l = 6.23$ MPa. Using (6) and the parameters stated in Table 2, the simulated deflection sensitivity is

$$\Psi_{\mathrm{PR,FEA}} = 1.88\,\mathrm{mV/nm}. \tag{11}$$

4. Instrumentation

An instrumentation amplifier read-out circuit was designed for high gain and bandwidth. A simplified diagram of the read-out circuit is shown in Fig. 4(a). The first stage provides buffering and differential gain, and the second stage provides common mode rejection. Texas Instruments OPA2211 opamps are chosen for the first-stage due to their low voltage noise of $e_n = 1.1\,\mathrm{nV}/\sqrt{\mathrm{Hz}}$ and sufficient bandwidth of 1.8 MHz at an overall differential gain of 21. The total output voltage is given by

$$V_o = \left(1 + \frac{2R_f}{R_g}\right) 100 V_d = A V_d \tag{12}$$

with additional ×100 post-amplification stages. A low noise bridge bias voltage is implemented using a LTC6655-1.25V precision voltage reference. Offset trimming of the Wheatstone bridge is achieved using the low noise bridge reference and an additional gain circuit connecting to the ref pin of the second stage. This approach avoids the need to implement potentiometers on the sensor bridge side of the circuit.

The noise of the circuit in Fig. 4(a) is dominated by the first gain stage, the equivalent circuit is shown in Fig. 4(b). The impedance seen by each amplifier input is $R_p/2$. The electrical noise is dictated by the noise sources shown in Fig. 4: Thermal noise in the piezoresistor R_p, feedback resistor R_f and R_g, op-amp voltage noise e_n and op-amp current noise $i_{n+/-}$. The bridge voltage reference V_b will also cause common mode noise to appear at both firs-stage amplifier inputs. The level of influence of this noise source at the output of the amplifier depends on the common mode rejection ratio (CMRR) of the second stage. With closely matched resistors R, a low-noise voltage reference source, and sufficiently high CMRR, the bridge excitation noise can be neglected.

The individual output noise spectral densities of the major noise sources can be written as (where $N_{x,y}(f) = \sqrt{S_{x,y}(f)}$ is the noise spectral density of the signal x due to a process y as a function of frequency f)

$$N_{v_{S+},R_p}(f) = e_{\frac{R_p}{2}} G_n \tag{13a}$$

$$N_{v_{S+},R_f}(f) = e_{R_f} \tag{13b}$$

$$N_{v_{S+},R_g}(f) = e_{R_g} \frac{R_f}{R_g} \tag{13c}$$

$$N_{v_{S+},e_n}(f) = e_n G_n \tag{13d}$$

$$N_{v_{S+},i_{n-}}(f) = i_{n-} R_f \tag{13e}$$

$$N_{v_{S+},i_{n+}}(f) = i_{n+} \frac{R_p}{2} G_n \tag{13f}$$

and are summarized in Table 3. The noise sources can be referred to an equivalent op-amp input noise voltage (RTI) or referred to output

Table 3
Summary of the noise terms in the equivalent non-inverting amplifier input stage shown in Fig. 4 using an OPA2211 with $R_g = 47.5\,\Omega$, $R_f = 470\,\Omega$, $R_p = 164.6\,\Omega$, $e_n = 1.1\,\text{nV}/\sqrt{\text{Hz}}$, $i_n = 1.7\,\text{pA}/\sqrt{\text{Hz}}$.

Noise source	RTI noise ($\text{nV}/\sqrt{\text{Hz}}$)	RTO noise ($\text{nV}/\sqrt{\text{Hz}}$)
Johnson noise $e_{\frac{R_p}{2}}$	1.15	24.0
Johnson noise e_{2R_f}	3.9	3.9
Johnson noise e_{R_g}	0.88	17.3
Op-amp voltage noise e_n	1.1	22.9
Op-amp current noise e_{ni-}	0.07	1.60
Op-amp current noise e_{ni+}	0.14	2.91
First stage noise $N_{v_{S+}}(f)$	1.82	37.8
Total noise $N_{v_o}(f)$	2.57	5340

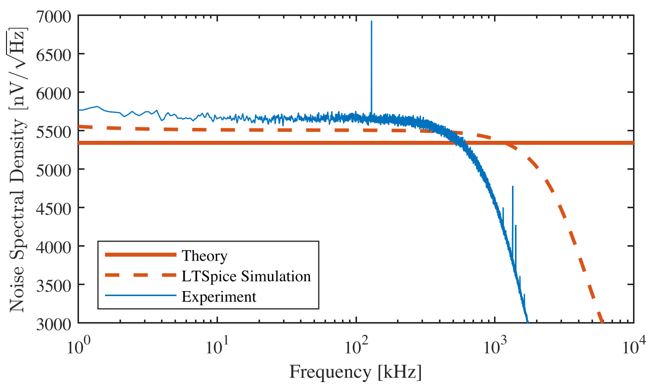

Fig. 5. Analytical, simulated and measured noise spectral densities of the custom instrumentation amplifier read-out configuration.

noise (RTO) by multiplying the RTI noise with the noise gain G_n of the circuit

$$G_n = 1 + \frac{2R_f}{R_g}. \tag{14}$$

The total output voltage noise spectral density is then obtained from summing the squares of each source stated in (13a)–(13f). Finally, the total noise of the custom-built instrumentation amplifier in Fig. 4(a) yields

$$N_{v_o}(f) = 100\sqrt{2}N_{v_{S+}}(f). \tag{15}$$

In Fig. 5, the total measured output voltage noise density is evaluated against an LTSpice simulation and the theoretical value predicted by (15). It can be seen that the experimentally determined noise floor is only marginally above the simulation. The total experimental electrical noise floor is approximately $N_e = 5680\,\text{nV}/\sqrt{\text{Hz}}$ at a total gain of $A = 2100$. The narrow-band peaks in the noise density between 100 kHz and 200 kHz are due to conducted and radiated electromagnetic interference from nearby switching power supplies. This noise is not intrinsic to the sensor or read-out circuit.

5. Experimental results

5.1. Fabrication

The PE-PR cantilever design was fabricated with the rapid MEMS prototyping process PiezoMUMPS® (MEMSCAP Inc.) and is depicted in Fig. 6. The process features a device layer of single-crystal-silicon with a thickness of 10 µm, a 0.5 µm layer of piezoelectric aluminum-nitrate (AlN) and a 1 µm layer of aluminum for electrical connections. The top surface of the device layer is doped by depositing a phosphosilicate glass layer and annealing in argon. This layer allows the direct implementation of a piezoresistive sensor on the top surface of the device layer without the requirement for an extra fabrication step, which maintains compatibility with the five mask PiezoMUMPS® process.

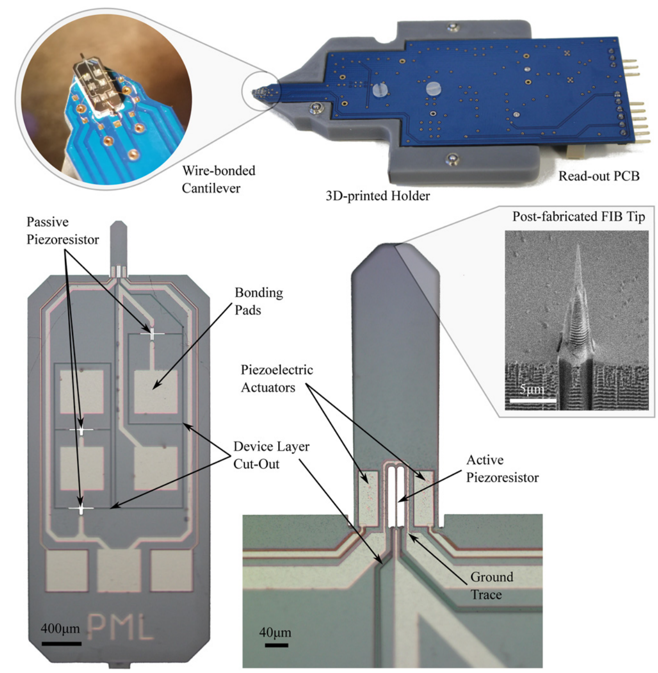

Fig. 6. Photos of the fabricated PE-PR cantilever with post-fabricated FIB tip and read-out circuit.

Since the PiezoMUMPS® process does not allow for the inclusion of sharp tips at the cantilever end, direct FIB deposition (FEI Helios Nanolab G3 CX DualBeam FIB/SEM) of Tungsten is used to form a multi-segment tip which is subsequently sharpened using tilted FIB milling [22]. A scanning electron micrograph image of the tip is shown in the inset in Fig. 6. The diameter of the tip base is approximately $d = 3\,\mu\text{m}$, the height $h = 12\,\mu\text{m}$, and the radius $r \approx 20\,\text{nm}$. The tips were fabricated by sequential deposition of multi-diameter Tungsten pillars where the diameter of the pillar is decreased toward the top [22]. In the last step, the tips of the deposited pillars were sharpened by focused ion beam milling. Using this approach, tip radii of sub 20 nm have been routinely achieved and used for AFM imaging [22,25]. While this process is not economical for mass production, the combination of a standard MEMS processing service and FIB tip fabrication is a straightforward and economical option for low volume production for research purposes.

The fabricated read-out circuit with a 3D-printed cantilever holder for a Horiba XploRA Nano Raman-AFM system is also shown in Fig. 6. The read-out circuit contains on-board low-noise power supplies (TPS7A4901 and TPS7A3001), a custom instrumentation amplifier (OPA2211), low noise precision bridge voltage reference (LTC6655-1.25V), offset trimming circuit and additional post amplification stages (OPA2209). The fabricated MEMS cantilever is wire-bonded directly onto the PCB in order to achieve the best performance.

5.2. Cantilever parameter calibration

A thermal noise calibration is performed to obtain values for the cantilever parameters of the first mode [45]. The measured thermal noise response using a laser Doppler vibrometer (Polytec, MSA-100-3D) and the corresponding Lorentzian function fit are shown in Fig. 7. From the fit, the resonance frequency is found to be $f_1 = 55.65\,\text{kHz}$, the quality factor $Q_1 = 531$, and modal stiffness is $k_1 =$

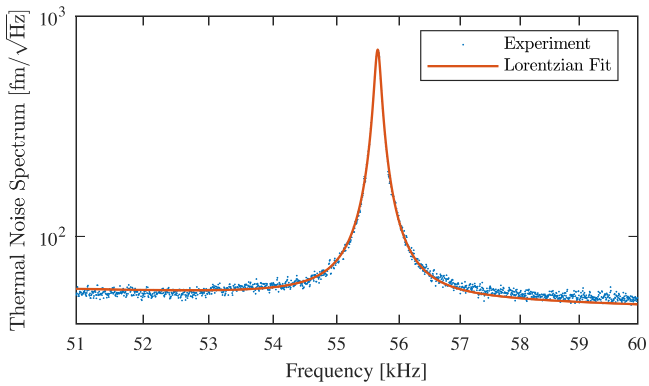

Fig. 7. Thermal noise spectrum of the fundamental mode of the PE-PR cantilever measured with a laser Doppler vibrometer (Polytec, MSA-100-3D) and Lorentzian function fit to the response to obtain the cantilever dynamic parameters.

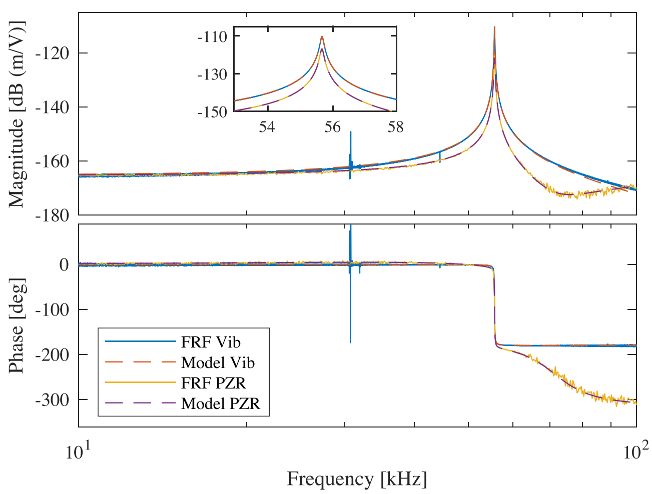

Fig. 8. Frequency response and identified models for the first mode of the PE-PR cantilever measured with a laser Doppler vibrometer (Vib) and using the piezoresistive sensor read-out (PZR). The inset shows a zoom on the first mode.

50.1 N/m. Details on the dynamic stiffness calibration using the thermal noise method are provided in Appendix B.

5.3. Frequency response

The frequency response of the PE-PR cantilever is measured by using a laser Doppler vibrometer (Polytec, MSA-100-3D) and by performing a sine sweep using a lock-in amplifier (Zurich Instruments, HF2LI) and the piezoresistive sensor read-out circuit. The measured responses as well as the corresponding identified models are shown in Fig. 8. The inset shows an excellent agreement between the two measured responses around the first mode. For the first mode of the cantilever, the response from actuation voltage V_i to displacement D measured with the MSA-100 is accurately predicted by a second order transfer function model as shown in Fig. 8. The piezoresistive read-out configuration yields a third order model which includes a first-order high-pass filter modeling the residual feedthrough from actuation voltage V_i to sensor output V_o. The sum of the mechanical second-order system with the high-pass feedthrough term yields a complex zero pair following the resonance. Equating the magnitude responses at the low-frequency point, yields an experimental deflection sensitivity of

$$\Psi_{\text{PR,exp}} = 1.74\,\text{mV/nm}. \tag{16}$$

Table 4
Summary of the cantilever parameters obtained from theory, finite element simulations, and experiment.

Parameter	Theory	Simulation	Experiment
f_1 [kHz]	55.04	56.55	55.65
Q_1	–	–	531
k_1 [N/m]	50.7	52.58	50.1
$\bar{\pi}_l$ [10^{-11} Pa^{-1}]	−26.27	–	−24.69
Ψ_{PR} [mV/nm]	1.60	1.88	1.74
N_{V_o} [nV/$\sqrt{\text{Hz}}$]	5340	5507	5680

5.4. Identification of the piezoresistive coefficient

The output of the piezoresistive sensor is given by substituting (6) in (12)

$$V_o \approx \frac{1}{4}\bar{\pi}_l\bar{\sigma}_l V_b A \tag{17}$$

where $A = 2100$ is the combined readout circuit gain. Since $\bar{\pi}_l$ is unknown and $\bar{\sigma}_l$ cannot be measured directly, the piezoresistive coefficient is estimated using the results from the finite element simulations in Section 3.3. Given the experimentally determined sensor sensitivity (16) and the average stress extracted along the piezoresistive sensing beam $\bar{\sigma}_l = 6.25$ MPa for an a amplitude of 580 nm, the effective longitudinal piezoresistive coefficient is determined to be

$$\bar{\pi}_l = -24.69 \times 10^{-11}\,\text{Pa}^{-1}. \tag{18}$$

This value is smaller than the theoretical value calculated in Section 3.2. The reduction in the piezoresistive coefficient is believed to be due to the unknown doping concentration and depth as well as temperature effects not modeled in the piezoresistor [37].

5.5. Discussion

A summary of the theoretical, simulated and experimentally verified cantilever, piezoresistor and circuit parameters are given in Table 4. All values are within acceptable tolerance values. Future work will focus on improving the effective longitudinal piezoresistive coefficient which will lead to a higher sensitivity and result in an improved noise response and lower relative feedthrough. In order to maintain compatibility with the PiezoMUMPS fabrication guidelines, methods from structural optimization [46] will be employed to optimize the size, location and orientation of the piezoresistor and the geometric shape of the cantilever. In comparison to other fully integrated cantilever design highlighted in Table 1, this work achieves a dynamic range of around 33 dB indicating a very low feedthrough.

6. AFM imaging

The hybrid piezoelectric-piezoresistive cantilever and readout circuit was interfaced with a Horiba XploRA Nano Raman-AFM system; a photo of the cantilever holder and PCB is shown in Fig. 6. Two samples were investigated in tapping mode at a 1 Hz line rate at 512 × 512 pixels using the fundamental eigenmode of the cantilever: a freshly cleaved Highly Oriented Pyrolytic Graphite (HOPG) sample and a blend of polystyrene (PS) and polyolefin elastomer (LDPE) (Bruker, PS-LDPE-12M).

The imaging results are shown in Figs. 9 and 10to which line fitting and plane leveling has been applied in post-processing. The first mode amplitude and setpoint was approximately 100 nm and 65 % for imaging the polymer sample and 30 nm and 85 % for imaging the HOPG sample. The higher free-air amplitude and lower setpoint for the polymer sample results in the excellent material contrast in the phase image. Despite some electronic noise visible

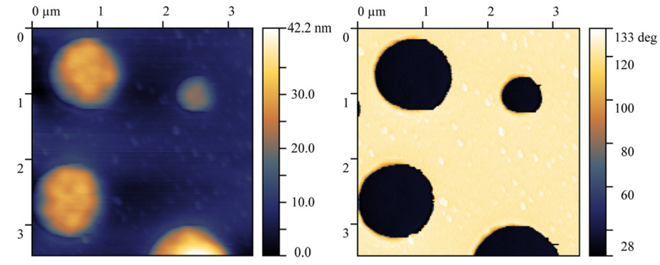

(a) Topography (b) Phase

Fig. 9. Tapping-mode AFM imaging results at the fundamental mode using the PE-PR cantilever showing (a) topography and (b) phase contrast of a polymer blend sample.

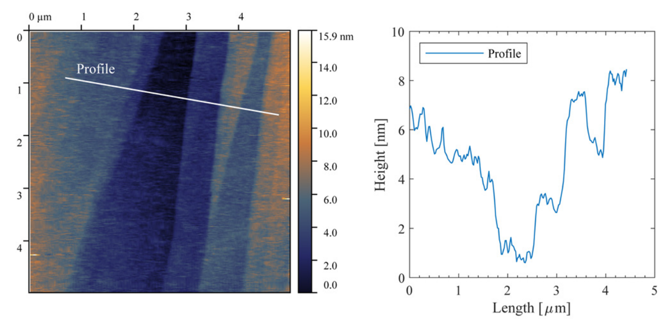

(a) Topography (b) Cross Section

Fig. 10. Tapping-mode AFM imaging results at the fundamental mode using the PE-PR cantilever showing (a) topography and (b) cross section profile of a HOPG sample.

in the image of the HOPG sample, the cross section in Fig. 10(b) clearly reveals the nanometer-sized steps.

7. Conclusion and future work

7.1. Conclusion

This works describes a hybrid piezoelectric-piezoresistive microcantilever design which can be fabricated using a standard commercial microfabrication process (PiezoMUMPS, MEMSCAP Inc.) without the need for an additional doping step to obtain the piezoresistor. The design utilizes a grounded piezoresistor, fabricated from the silicon device layer, in a quarter-bridge configuration. Using matched on-chip passive piezoresistors, a low feedthrough from piezoelectric actuation to piezoresistive sensing is achieved. The theoretical sensor sensitivity, based on Euler-Bernoulli beam theory, is compared to finite element simulations and experimental results obtained from a fabricated prototype cantilever.

The fixed device layer thickness of 10 μm of the Piezo-MUMPS process constitutes a certain limitation to the feasible cantilever dimensions using this process. In this work, the cantilever dimensions were chosen such that the resulting dynamic stiffness of the fundamental mode matches commercial stiff tapping-mode cantilevers. These stiffer cantilevers are best suited for medium to hard samples and provide a benefit for sticky samples such as polymers. For nanomechanical mapping such as modulus and deformation measurements, the cantilever stiffness should be matched with the sample stiffness. Therefore, stiffer cantilevers are ideally suited to measure samples with Young's moduli in the order of 100 MGa to 100 GPa. This stiffness range encompasses samples such as polymers, plastics, ceramics, and metals.

7.2. Future work

The proposed active cantilever design has significant potential for future work including surface passivation for operation in liquid environments and optimization of the sensor location for multifrequency atomic force microscopy [22]. Most importantly, the proposed integrated piezoresistive sensor has the potential to measure the cantilever deflections down to DC as opposed to piezoelectric sensing configurations which result in a high-pass configuration [47]. This advantage will be utilized in ongoing research to extend the imaging capabilities to advanced imaging modes such as peak force tapping mode.

Lastly, the authors are currently working toward integrating the tip fabrication step into the commercial MEMS fabrication process. While post-fabricating sharp tips using FIB deposition and milling has been demonstrated to yield excellent proof-of-concept AFM imaging capabilities [13,22,28,25,29], the full economic benefit is reached by integrating isotropically etched Si tips in the fabrication process.

Author contributions

Michael Ruppert: Conceptualization, methodology, software, validation, formal analysis, investigation, writing – original draft, visualization, project administration. Yuen Yong: Funding acquisition, writing – reviewing and editing. Andrew Fleming: Supervision, investigation, writing – reviewing and editing.

Appendix A. Analytical piezoresistive deflection sensitivity

In the following, we assume an Euler-Bernoulli beam with homogeneous isotropic linear elastic material with constant cross section in pure bending. This assumption implies a linearly varying stress distribution throughout the beam and enables an analytical sensor equation to be derived. For an ideal device, the surface stress along the x direction is given by Hooke's law as

$$\sigma_l(x) = -\frac{t}{2}Ez''(x), \tag{19}$$

where t is the cantilever thickness and E is the Young's modulus. $z''(x)$ is the second derivative of the displacement which can be written as a function of the tip deflection $z(l)$ as [43]

$$z''(x) = \frac{3}{l^3}(l-x)z(l) \tag{20}$$

where l is the cantilever length. The surface bending stress is maximum at the base of the cantilever

$$\sigma_l(0) = -\frac{3tE}{2l^2}z(l). \tag{21}$$

For a real device, due to the finite length of the piezoresistor l_p, the average stress is [48]

$$\bar{\sigma}_l = \frac{1}{l_p}\int_0^{l_p}\sigma_l(x)dx = \frac{tE}{2l_p}\int_0^{l_p} z''(x)dx = \frac{tE}{2l_p}z'(l_p) \tag{22}$$

where

$$z'(l_p) = \frac{3l_p}{2l^3}(2l-l_p)z(l). \tag{23}$$

Using (23) and (22), the average stress is given by

$$\bar{\sigma}_l = \frac{3tE}{4l^3}(2l-l_p)z(l) \tag{24}$$

and the output sensing voltage is found to be

$$V_d = \frac{1}{4}\bar{\pi}_l\frac{3tE}{4l^3}(2l-l_p)z(l)V_b. \tag{25}$$

Appendix B. Dynamic stiffness calibration using the thermal noise method

Experimentally, the thermal stiffness calibration is performed by measuring the velocity power spectrum at the end of the cantilever using a laser Doppler vibrometer (Polytec, MSA-100-3D) with the piezoelectric layers grounded and integrating the area underneath the resonance peak [45]. This is done by performing a Lorentzian function fit to the measured thermal noise response of the form [49]

$$S(f) = \frac{Af_0^4}{Q^2(f^2 - f_0^2)^2 + f^2 f_0^2} + A_0, \tag{26}$$

where A is a fitting parameter and A_0 is the white background noise. From the fit, the mean squared velocity can be extracted as

$$\bar{v}^2 = \frac{\pi f_0 A}{2Q} \tag{27}$$

which allows to calculate the spring constant as

$$k = (2\pi f_0)^2 \frac{k_B T}{\bar{v}^2}. \tag{28}$$

Declaration of Competing Interest

The authors report no declarations of interest.

References

[1] G. Binnig, C.F. Quate, C. Gerber, Atomic force microscope, Phys. Rev. Lett. 56 (1986) 930–933, http://dx.doi.org/10.1103/PhysRevLett.56.930.
[2] M. Gentili, C. Giovannella, S. Selci, Nanolithography – A Borderland between STM, EB, IB, and X-Ray Lithographies, vol. 264, Springer Netherlands, 1994, http://dx.doi.org/10.1007/978-94-015-8261-2.
[3] P. Vettiger, G. Cross, M. Despont, U. Drechsler, U. Durig, B. Gotsmann, W. Haberle, M.A. Lantz, H.E. Rothuizen, R. Stutz, G.K. Binnig, The “millipede” – nanotechnology entering data storage, IEEE Trans. Nanotechnol. 1 (1) (2002) 39–55, http://dx.doi.org/10.1109/TNANO.2002.1005425.
[4] L. Gross, F. Mohn, N. Moll, P. Liljeroth, G. Meyer, The chemical structure of a molecule resolved by atomic force microscopy, Science 325 (5944) (2009) 1110–1114.
[5] D. Ebeling, M. Šekutor, M. Stiefermann, J. Tschakert, J.E. Dahl, R.M. Carlson, A. Schirmeisen, P.R. Schreiner, Assigning the absolute configuration of single aliphatic molecules by visual inspection, Nat. Commun. 9 (2420) (2018).
[6] E.S. Parsons, G.J. Stanley, A.L. Pyne, A.W. Hodel, A.P. Nievergelt, A. Menny, A.R. Yon, A. Rowley, R.P. Richter, G.E. Fantner, et al., Single-molecule kinetics of pore assembly by the membrane attack complex, Nat. Commun. 10 (1) (2019) 2066.
[7] B. Bhushan, Springer Handbook of Nanotechnology, Springer-Verlag Berlin Heidelberg, 2010.
[8] G. Meyer, N.M. Amer, Novel optical approach to atomic force microscopy, Appl. Phys. Lett. 53 (12) (1988) 1045–1047, http://dx.doi.org/10.1063/1.100061.
[9] M.G. Ruppert, S.O.R. Moheimani, High-bandwidth multimode self-sensing in bimodal atomic force microscopy, Beilstein J. Nanotechnol. 7 (2016) 284–295, http://dx.doi.org/10.3762/bjnano.7.26.
[10] R. Pedrak, T. Ivanov, K. Ivanova, T. Gotszalk, N. Abedinov, I.W. Rangelow, K. Edinger, E. Tomerov, T. Schenkel, P. Hudek, Micromachined atomic force microscopy sensor with integrated piezoresistive sensor and thermal bimorph actuator for high-speed tapping-mode atomic force microscopy phase-imaging in higher eigenmodes, J. Vac. Sci. Technol. B 21 (6) (2003) 3102–3107, http://dx.doi.org/10.1116/1.1614252.
[11] P.-F. Indermühle, G. Schürmann, G.-A. Racine, N. de Rooij, Fabrication and characterization of cantilevers with integrated sharp tips and piezoelectric elements for actuation and detection for parallel AFM applications, Sens. Actuators A 60 (1–3) (1997) 186–190, http://dx.doi.org/10.1016/S0924-4247(96)01440-9.
[12] N. Sarkar, G. Lee, D. Strathearn, M. Olfat, R.R. Mansour, A multimode single-chip scanning probe microscope for simultaneous topographical and thermal metrology at the nanometer scale, in: 2016 IEEE 29th International Conference on Micro Electro Mechanical Systems (MEMS), Shanghai, China, 2016, pp. 55–58.
[13] M.G. Ruppert, A.G. Fowler, M. Maroufi, S.O.R. Moheimani, On-chip dynamic mode atomic force microscopy: a silicon-on-insulator MEMS approach, IEEE J. Microelectromech. Syst. 26 (1) (2017) 215–225.
[14] R. Kassies, K.O. van der Werf, M.L. Bennink, C. Otto, Removing interference and optical feedback artifacts in atomic force microscopy measurements by application of high frequency laser current modulation, Rev. Sci. Instrum. 75 (3) (2004) 689–693, http://dx.doi.org/10.1063/1.1646767.
[15] Y. Sarov, A. Frank, T. Ivanov, J.-P. Zöllner, K. Ivanova, B. Volland, I.W. Rangelow, A. Brogan, R. Wilson, P. Zawierucha, M. Zielony, T. Gotszalk, N. Nikolov, M. Zier, B. Schmidt, I. Kostic, Parallel proximal probe arrays with vertical interconnections, J. Vac. Sci. Technol. B 27 (6) (2009) 3132–3138, http://dx.doi.org/10.1116/1.3256662.
[16] T. Itoh, T. Suga, Development of a force sensor for atomic force microscopy using piezoelectric thin films, Nanotechnology 4 (4) (1993) 218 http://stacks.iop.org/0957-4484/4/i=4/a=007.
[17] M. Tortonese, R.C. Barrett, C.F. Quate, Atomic resolution with an atomic force microscope using piezoresistive detection, Appl. Phys. Lett. 62 (8) (1993) 834–836, http://dx.doi.org/10.1063/1.108593.
[18] I.W. Rangelow, T. Ivanov, A. Ahmad, M. Kaestner, C. Lenk, I.S. Bozchalooi, F. Xia, K. Youcef-Toumi, M. Holz, A. Reum, Active scanning probes: a versatile toolkit for fast imaging and emerging nanofabrication, J. Vac. Sci. Technol. B 35 (6) (2017) 06G101, http://dx.doi.org/10.1116/1.4992073.
[19] A. Schneider, R.H. Ibbotson, R.J. Dunn, E. Huq, Arrays of su-8 microcantilevers with integrated piezoresistive sensors for parallel AFM applications, Microelectron. Eng. 88 (8) (2011) 2390–2393, http://dx.doi.org/10.1016/j.mee.2010.11.047.
[20] M. Dukic, J.D. Adams, G.E. Fantner, Piezoresistive AFM cantilevers surpassing standard optical beam deflection in low noise topography imaging, Sci. Rep. 5 (16393) (2015) 1–11, http://dx.doi.org/10.1038/srep16393.
[21] S.I. Moore, M.G. Ruppert, Y.K. Yong, Multimodal cantilevers with novel piezoelectric layer topology for sensitivity enhancement, Beilstein J. Nanotechnol. 8 (2017) 358–371 http://www.precisionmechatronicslab.com/wp-content/uploads/2017/02/2190-4286-8-38.pdf.
[22] M.G. Ruppert, S.I. Moore, M. Zawierta, A.J. Fleming, G. Putrino, Y.K. Yong, Multimodal atomic force microscopy with optimized higher eigenmode sensitivity using on-chip piezoelectric actuation and sensing, Nanotechnology 30 (8) (2019) 085503, http://dx.doi.org/10.1088/1361-6528/aae40b.
[23] M.G. Ruppert, Y.K. Yong, Note: Guaranteed collocated multimode control of an atomic force microscope cantilever using on-chip piezoelectric actuation and sensing, Rev. Sci. Instrum. 88 (8) (2017) 086109, http://dx.doi.org/10.1063/1.4990451.
[24] M.B. Coskun, A.G. Fowler, M. Maroufi, S.O.R. Moheimani, On-chip feedthrough cancellation methods for microfabricated AFM cantilevers with integrated piezoelectric transducers, IEEE J. Microelectromech. Syst. 26 (6) (2017) 1287–1297, http://dx.doi.org/10.1109/JMEMS.2017.2731762.
[25] S.I. Moore, M.G. Ruppert, Y.K. Yong, AFM cantilever design for multimode Q control: arbitrary placement of higher-order modes, IEEE/ASME Trans. Mechatron. (2020) 1–6, http://dx.doi.org/10.1109/TMECH.2020.2975627 (early access).
[26] J.-Y. Lee, A. Seshia, Parasitic feedthrough cancellation techniques for enhanced electrical characterization of electrostatic microresonators, Sens. Actuators A 156 (1) (2009) 36–42, http://dx.doi.org/10.1016/j.sna.2009.02.005.
[27] M.G. Ruppert, S.O.R. Moheimani, A novel self-sensing technique for tapping-mode atomic force microscopy, Rev. Sci. Instrum. 84 (12) (2013) 125006, http://dx.doi.org/10.1063/1.4841855.
[28] M.B. Coskun, H. Alemansour, A.G. Fowler, M. Maroufi, S.O.R. Moheimani, Q control of an active AFM cantilever with differential sensing configuration, IEEE Trans. Control Syst. Technol. 27 (5) (2019) 2271–2278, http://dx.doi.org/10.1109/TCST.2018.2850338.
[29] M. Mahdavi, M.B. Coskun, S.O.R. Moheimani, High dynamic range AFM cantilever with a collocated piezoelectric actuator-sensor pair, IEEE J. Microelectromech. Syst. 29 (21) (2020) 260–267, http://dx.doi.org/10.1109/JMEMS.2020.2967794.
[30] S. Minne, S. Manalis, C. Quate, Parallel atomic force microscopy using cantilevers with integrated piezoresistive sensors and integrated piezoelectric actuators, Appl. Phys. Lett. 67 (26) (1995) 3918–3920, http://dx.doi.org/10.1063/1.115317.
[31] G.E. Fantner, D.J. Burns, A.M. Belcher, I.W. Rangelow, K. Youcef-Toumi, DMCMN: in depth characterization and control of AFM cantilevers with integrated sensing and actuation, J. Dyn. Syst. Meas. Control Trans. ASME 131 (6) (2009) 061104, http://dx.doi.org/10.1115/1.4000378.
[32] T. Michels, E. Guliyev, M. Klukowski, I.W. Rangelow, Micromachined self-actuated piezoresistive cantilever for high speed SPM, Microelectron. Eng. 97 (2012) 265–268.
[33] M. Maroufi, A. Bazaei, A. Mohammadi, S.O.R. Moheimani, Tilted beam piezoresistive displacement sensor: design, modeling, and characterization, IEEE J. Microelectromech. Syst. 24 (5) (2015) 1594–1604 http://reza.moheimani.org/lab/wp-content/uploads/J15j.pdf.
[34] M.G. Ruppert, Y.K. Yong, Design of hybrid piezoelectric/piezoresistive cantilevers for dynamic-mode atomic force microscopy, 2018 IEEE/ASME International Conference on Advanced Intelligent Mechatronics (AIM) (2018) 144–149, http://dx.doi.org/10.1109/AIM.2018.8452229.
[35] A. Cowen, G. Hames, K. Glukh, B. Hardy, PiezoMUMPs Design Handbook, 1st edition, MEMSCAP Inc., 2014.
[36] J.C. Doll, B.L. Pruitt, Piezoresistor Design and Applications, Springer, 2013.
[37] S.J. Park, J.C. Doll, B.L. Pruitt, Piezoresistive cantilever performance; part I: analytical model for sensitivity, piezoresistive, IEEE J. Microelectromech. Syst. 19 (1) (2010) 137–148, http://dx.doi.org/10.1109/JMEMS.2009.2036581.
[38] W.-T. Park, Piezoresistivity, Springer Netherlands, Dordrecht, 2012, pp. 2111–2117, http://dx.doi.org/10.1007/978-90-481-9751-4_222.

[39] C.S. Smith, Piezoresistance effect in germanium and silicon, Phys. Rev. 94 (1954) 42–49, http://dx.doi.org/10.1103/PhysRev.94.42.
[40] M.A. Hopcroft, W.D. Nix, T.W. Kenny, What is the young's modulus of silicon? J. Microelectromech. Syst. 19 (2) (2010) 229–238, http://dx.doi.org/10.1109/JMEMS.2009.2039697.
[41] G.E. Fantner, W. Schumann, R.J. Barbero, A. Deutschinger, V. Todorov, D.S. Gray, A.M. Belcher, I.W. Rangelow, K. Youcef-Toumi, Use of self-actuating and self-sensing cantilevers for imaging biological samples in fluid, Nanotechnology 20 (43) (2009) 434003 http://stacks.iop.org/0957-4484/20/i=43/a=434003.
[42] T. Gotszalk, P. Grabiec, I.W. Rangelow, Piezoresistive sensors for scanning probe microscopy, Ultramicroscopy 82 (1–4) (2000) 39–48, http://dx.doi.org/10.1016/S0304-3991(99)00171-0.
[43] J. Gere, S. Timoshenko, Mechanics of Materials, PWS Publishing Company, 1997.
[44] S. Ilanko, L. Monterrubio, Y. Mochida, The Rayleigh-Ritz Method for Structural Analysis, John Wiley & Sons, 2014.
[45] M.G. Ruppert, N.F.S.D. Bem, A.J. Fleming, Y.K. Yong, Characterization of active microcantilevers using laser Doppler vibrometry, in: 18th Asian Pacific Vibration Conference, Sydney, Australia, 2019.
[46] S.I. Moore, M.G. Ruppert, Y.K. Yong, An optimization framework for the design of piezoelectric AFM cantilevers, Precis. Eng. 60 (2019) 130–142, http://dx.doi.org/10.1016/j.precisioneng.2019.08.005.
[47] M.G. Ruppert, S.O.R. Moheimani, Novel reciprocal self-sensing techniques for tapping-mode atomic force microscopy, in: Proc. 19th IFAC World Congress, IFAC, Cape Town, South Africa, 2014, pp. 7474–7479.
[48] O. Hansen, A. Boisen, Noise in piezoresistive atomic force microscopy, Nanotechnology 10 (1) (1999) 51.
[49] J.E. Sader, J.A. Sanelli, B.D. Adamson, J.P. Monty, X. Wei, S.A. Crawford, J.R. Friend, I. Marusic, P. Mulvaney, E.J. Bieske, Spring constant calibration of atomic force microscope cantilevers of arbitrary shape, Rev. Sci. Instrum. 83 (10) (2012) 103705, http://dx.doi.org/10.1063/1.4757398.

Biographies

Michael G. Ruppert received the Dipl.-Ing. degree in automation technology from the University of Stuttgart, Germany, in 2013 and the PhD degree in Electrical Engineering from The University of Newcastle, Australia in 2017. As a visiting researcher, he was with The University of Texas at Dallas, USA from 2015 until 2016 and he is currently a postdoctoral research fellow at The University of Newcastle. His research interests include the utilization of system theoretic tools for sensing, estimation and control in high-speed and multifrequency atomic force microscopy. Dr Ruppert's research has been recognized with the 2019 Best Conference Paper Award at the 2019 International Conference on Manipulation, Automation and Robotics at Small Scales (MARSS), the 2018 IEEE Transactions on Control Systems Technology Outstanding Paper Award, and the 2017 University of Newcastle Higher Degree by Research Excellence Award.

Andrew J. Fleming (M'02) received the B.Sc. degree in electrical engineering and the Ph.D. degree in mechatronics engineering from the University of Newcastle, Callaghan, NSW, Australia, in 2000 and 2004,respectively. He is currently an Australian Research Council Future Fellow and the Director with the Precision Mechatronics Lab, University of Newcastle. He is the co-author of three books, and more than 180 journal and conference articles. He is the Inventor of several patent applications. His research interests include lithography, nanopositioning, scanning probe microscopy, and biomedical devices. Dr. Fleming received the Academy for Technological Sciences and Engineering Baterham Medal in 2016, the Newcastle Innovation Rising Star Award for Excellence in Industrial Engagement in 2012, the IEEE Control Systems Society Outstanding Paper Award in 2007, and the University of Newcastle Researcher of the Year Award in 2007.

Yuen K. Yong received the Bachelor of Engineering degree in Mechatronics Engineering and the PhD degree in Mechanical Engineering from The University of Adelaide, Australia, in 2001 and 2007, respectively. She is current an associate professor at The University of Newcastle, Australia. Her research interests include nanopositioning systems, design and control of microcantilevers, atomic force microscopy, and miniature robotics. Dr Yong was an Australian Research Council DECRA fellow from 2013 to 2017. She is an associate editor for the IEEE/ASME Transactions of Mechatronics. She was the recipient of the University of Newcastle Vice-Chancellor's Award for Research Excellence in 2014 and the Vice-Chancellor's Award for Research Supervision Excellence in 2017.